2017

Filament Wavefront Evolution

Daniel Thul
University of Central Florida

FILAMENT WAVEFRONT EVOLUTION

by

DANIEL J. THUL
B. S. Rose-Hulman Institute of Technology, 2015

A thesis submitted in partial fulfillment of the requirements
for the degree of Master of Science
in the College of Optics and Photonics
at the University of Central Florida
Orlando, Florida

Summer Term
2017

Major Professor: Martin C. Richardson

ABSTRACT

Filamentation is a complex process that gives rise to many nonlinear interactions. However, the fundamentals of filament formation and propagation can be explained in terms of two dominant mechanisms: Kerr self-focusing and plasma defocusing. The first to occur, self-focusing, is responsible for an increase in irradiance through beam collapse. This process requires sufficient initial peak power, on the order of gigawatts for near infrared beams in air. Plasma defocusing then arrests the collapse process once the irradiance reaches the ionization threshold of the medium. These two processes balance each other in an extended plasma channel known as a filament. A beam's collapse behavior is strongly influenced by the initial beam conditions, especially in applications that require power scaling to terawatt levels where the Kerr effect is more pronounced. Therefore, understanding and controlling the collapse process is essential in this regime. For this reason, an exploration of the wavefront evolution of filamenting beams is of great interest and the topic of this thesis, which has three parts. First, it reviews the filamentation process and describes characteristics of filaments. Next, experimental measurements of the wavefronts of filamenting beams are given in two separate regimes. The first regime is the Kerr self-focusing that takes place before beam collapse is arrested. This data is then contrasted with wavefront measurements within a filament after collapse has occurred.

ACKNOWLEDGMENTS

I would like to thank my advisors, Dr. Richardson, Dr. Shah, and Dr. Baudelet, for the assistance and insights provided during the course of this work. I'd also like to thank Dr. Shermineh Rostami for her experimental advice and feedback during the thesis writing process. I am grateful for all the support I received from the entire LPL group, especially from those on the filamentation team. This work was funded by by HEL/JTO MRI "Fundamentals of filamentation interaction," ARO MURI "Light filamentation science," and the State of Florida.

TABLE OF CONTENTS

LIST OF FIGURES

LIST OF ACRONYMS

BPP	–	Beam parameter product
FWM	–	Four-wave mixing
MI	–	Modulation instability
MPA	–	Multi-photon absorption
MPI	–	Multi-photon ionization
MTFL	–	Multi-terawatt femtosecond laser
PV	–	Peak-to-valley
PS	–	Periscope
SPM	–	Self-phase modulation
SHWFS	–	Shack-Hartmann wavefront sensor
SC	–	Supercontinuum
TI	–	Tunneling ionization
USP	–	Ultra-short pulse

CHAPTER 1: FILAMENTATION

1.1 Basic Physical Processes: Kerr and Plasma Nonlinearities

Filamentation begins with self-focusing. The original work on this process showed that self-trapping at optical frequencies occurs when the Kerr nonlinearity balances diffraction [1]. Here, a beam is able to travel without changing form in what is known as a Townes profile. Further theory dealt with beams where self-focusing overcomes diffraction [2]. These early works define the critical power as that required for self-focusing to occur. Its formula, still used today, is given generally in Eq. 1.1. Here, λ_0 denotes the vacuum wavelength, n_0 is the linear refractive index, n_2 is the Kerr coefficient, and α is a unitless parameter that varies based on the input beam shape, ~1.9 for a Gaussian beam [3]. A typical value of n_2 is $\sim 2 \cdot 10^{-19}\, cm^2/W$ for air [4, 5]. It should be noted that this formula was originally derived for continuous beams and only gives a rough approximation in the USP regime [6]. Gaussian beams with power P above this limit will collapse at a location given in Eq. 1.2. The quantity $z_r = \frac{kw_0^2}{2}$ denotes the Rayleigh range of the beam, where $k = n_0 k_0 = n_0 \frac{2\pi}{\lambda_0}$ and w_0 is the 1/e^2 radius of the beam's intensity [7, 8]. Different estimates are required for non-Gaussian beams [9]. As expected, collapse distance decreases as beam power increases.

$$P_{cr} = \alpha \frac{\lambda_0^2}{4\pi n_0 n_2} \tag{1.1}$$

$$L_c = \frac{0.367 z_r}{\sqrt{\left[\left(\frac{P}{P_{cr}}\right)^{\frac{1}{2}} - 0.852\right]^2 - 0.0219}} \tag{1.2}$$

The value of P_{cr} for a Gaussian beam at 800 nm in air is just under 5 GW. When $P = 10P_{cr}$, the corresponding L_c is approximately 35 meters for a beam diameter (1/e^2) of 15 mm. The critical power scales with the square of wavelength because a stronger nonlinearity is needed for collapse when diffraction strength is increased. The value of P_{cr} is also reduced in materials with larger Kerr coefficients. The collapse location is proportional to the Rayleigh length of the beam, which scales with the square of beam diameter. This is expected because irradiance will be reduced for large area beams, thus limiting the nonlinear index modifications. In the case of collapse, a beam's irradiance will increase along propagation, eventually becoming large enough for optically induced ionization to take place. Plasma generation then causes a reduction in the local refractive index, thus countering the self-focusing effect and arresting the collapse process. The competition between the Kerr and plasma contributions to the refractive index is given in Eq. 1.3 [10].

$$n(r,t) = n_0 + n_2 I(r,t) - \frac{\rho(r,t)}{2\rho_c} \tag{1.3}$$

The Kerr coefficient, also known as the nonlinear refractive index, is defined as $n_2 = \frac{3\chi^{(3)}}{4\varepsilon_0 c n_0^2}$ where $\chi^{(3)}$ is the third-order material susceptibility, ε_0 is the permittivity of free-space, and c is the speed of light in vacuum. The critical plasma density $\rho_c = \frac{\varepsilon_0 m_e \omega_0^2}{e^2}$ is approximately $2 \cdot 10^{21} cm^{-3}$ for 800 nm light. This measure represents the density at which the plasma becomes opaque for an angular frequency $\omega_0 = ck_0$. The parameters m_e and e are the electron mass and charge, respectively. The short time scales and large intensities of femtosecond pulses reside in a regime where multi-photon ionization (MPI) and tunneling ionization (TI) are responsible for plasma generation, rather than the avalanche process

[10, 11]. The MPI process occurs when several photons are required for ionization. The photon energy at 800 nm is ~1.55 eV. In air, oxygen is the dominant contributor to plasma generation through this process. Its ionization potential is U_i~12 eV and 8 photons at 800 nm contribute through multi-photon absorption (MPA) to overcome this threshold. Thus, the ionization rate is proportional to I^8. Nitrogen has a larger ionization potential of U_i~15.6 eV and its contribution to MPI is negligible [12]. The process of TI requires higher intensities that MPI. Here, the Coulomb potential is reduced by the external field, making it more probable for an electron to escape through the tunneling process. Both processes are illustrated schematically in Fig. 1.1.

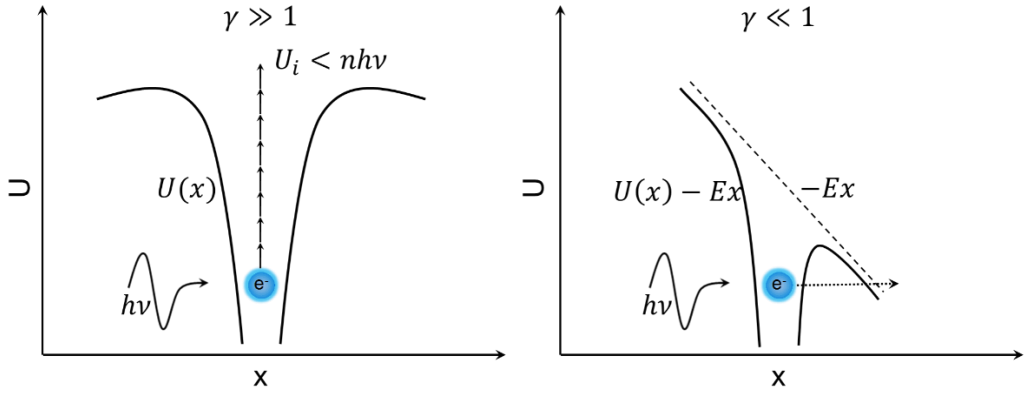

Figure 1.1 – The processes of MPI and TI are shown qualitatively on the left and right, respectively. The MPI process requires absorption of several photons for an electron to overcome the Coulomb potential. At higher intensities, the field is able to distort the potential enough such that electron tunneling becomes probable.

The relative contributions of MPI and TI are determined by the Keldysh parameter, defined in Eq. 1.4 [13]. The MPI process dominates when $\gamma \gg 1$ and TI dominates when $\gamma \ll 1$. This equation shows that much larger intensities are required for TI to overtake MPI, allowing TI to potentially be ignored [14].

$$\gamma = \frac{\omega_0}{e}\sqrt{\frac{m_e U_i n_0 c \varepsilon_0}{I}} \tag{1.4}$$

When $\frac{\rho(r,t)}{2\rho_c} > n_2 I(r,t)$, there is a negative net contribution to the refractive index according to Eq. 1.3 and defocusing occurs. This causes the irradiance to decrease, thus reducing the ionization rate. Eventually, the reduction of the plasma density allows the self-focusing process to take over and restart the cycle. Repetitive Kerr self-focusing and plasma defocusing cycles create an extended plasma channel, illustrated in Fig. 1.2. This causes the beam to be self-guided over several Rayleigh lengths in what is known as a filament.

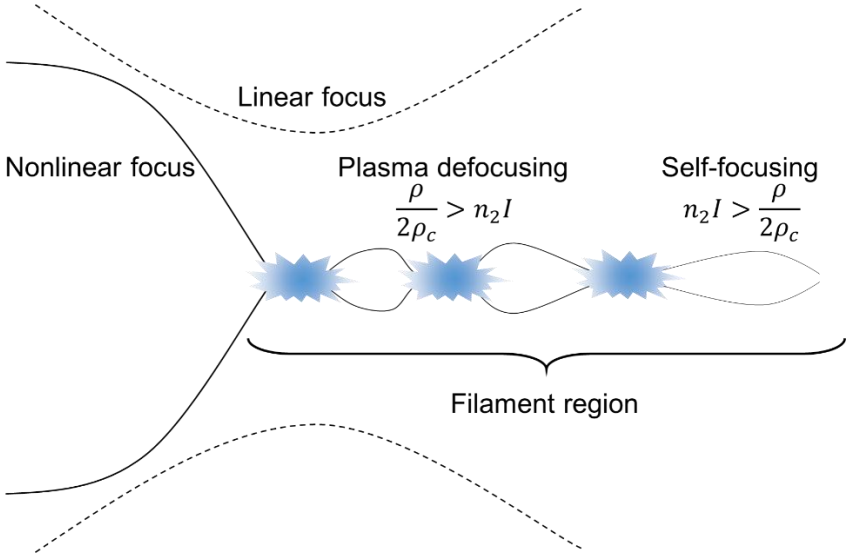

Figure 1.2 – A filamenting beam is qualitatively compared to a beam focused in the linear regime. In the filament region, a dynamic balance between Kerr and plasma nonlinearities sustains a confined plasma channel over long distances.

1.2 Filament Characteristics

The first observations of nonlinear optical phenomena came shortly after the invention of the Q-switched laser [15]. The availability of high power optical pulses enabled the initial investigations of nonlinear self-focusing. The first experiments were performed in media with large Kerr coefficients where it's easier to achieve collapse. One of the first nonlinear processes observed was self-trapping [16]. This result confirmed the theoretical trapping

threshold power and trapping length [2]. Additionally, the trapped profile qualitatively matched the Townes profile [1]. Other works explored the relationship between the filament structure and nonlinear effects. For example, self-focusing was seen to amplify stimulated Brillouin and Raman scattering [17-21]. Filaments were also seen to modify degenerate four-wave mixing (FWM) patterns [22]. These three processes are relatively similar in concept. Brillouin scattering is a three-wave process in which an optical wave inelastically scatters with a matter wave, producing a third wave at a new frequency [23]. It is most common to consider matter waves as quantized thermal oscillations. These quantized vibrations are represented as quasi-particles, deemed acoustic phonons [24]. Raman scattering is identical, except the incoming optical wave scatters with an optical phonon, which represents molecular rotations and vibrations [24, 25]. The process of FWM allows three optical waves to scatter, creating a fourth frequency. This process differs from the first two in that it is passive. The energy is coupled through virtual states, rather than being fed into the medium [24]. Enhancements and modifications to these effects were seen to modify the filament, including temporal break-up and spatial formation of multiple ‘hot’ filaments with diameters ranging from ~5 to 50 μm [26]. Spatial break-up of filaments was observed in a seemingly random fashion. One explanation attributed this behavior to modulation instability (MI) [27, 28]. This analysis showed that certain spatial frequencies are unstable and receive gain when the beam is subjected to small perturbations. Random noise acts as a seed for MI, potentially directing the multi-filament pattern. Another interesting feature observed was super-continuum (SC) generation. Here, filaments were shown to produce spectral broadening through self-phase

modulation (SPM) [29, 30]. The SPM process is the temporal analogue of Kerr self-focusing. Refractive index variations follow the temporal shape of the pulse. The leading edge experiences a growing index while the opposite is true for the trailing edge. Since $\delta\omega_0 \propto -\delta n_0$, the frequency is decreased and increased at the leading and trailing edges, respectively. Thus, spectral components are added to both sides of the initial spectrum [29]. This broadening was enhanced to 300 nm in width when non-degenerate FWM was first demonstrated [31]. Frequencies above and below the input beam were generated due to nonlinear frequency mixing within the filament. These frequencies were emitted in a cone, a pattern now referred to as “conical emission” [32]. This feature, shown in Fig. 1.3, is now a trademark of filamentation.

Figure 1.3 – Conical emission is as typical feature of filaments. This pattern, shown above, is generated along filament propagation [32].

These were the first signs of ‘filament’ formation, even though this term is thought of in a different context today. Early efforts used nanosecond and picosecond pulses and could only produce short filaments (on the order of a few inches) in media with large Kerr coefficients. The possibility of generating extended filaments came later, when femtosecond pulses were used to produce plasma channels over ranges exceeding 20 m in air [33]. This possibility was facilitated by the invention of chirp-pulse amplification of USP lasers,

greatly increasing achievable peak powers [34]. Filamentation in this regime is the focus of this study. The effects produced are reminiscent of those seen in early experiments.

The most basic feature of a femtosecond filament is its spatial structure, as was the case in the pico- and nanosecond regimes. Typical single filament core diameters are no larger than 300-400 μm during the self-guiding process for 800 nm femtosecond pulses [35]. However, the core only contains about 10% of a filament's energy. A significant portion is carried in a peripheral energy reservoir, also known as a photon bath, that extends as far as 2 mm in diameter [36, 37, 38]. This core-reservoir structure exists once collapse has been established and persists along propagation. The distribution in this regime also matches the theoretical Townes profile, even though this prediction was first applied to continuous sources [1, 38]. Self-consistent formation of the Townes profile is even quantitatively achieved for different initial beam profiles [39]. Since this structure persists along the plasma channel, it makes sense that peak intensity and plasma density would also be conserved. This feature is termed "intensity clamping" and is a direct consequence of the self-guiding induced by the balance of the Kerr effect and MPI [40-42]. As described in the previous section, the ionization rate in air is proportional to I^8 in the presence of femtosecond pulses. Thus, the large intensities produced during self-focusing result in drastic increases in the ionization rate. This sudden onset of plasma halts self-focusing through MPA and plasma defocusing, clamping the beam intensity at a peak value. Typical clamping intensity values are $10^{13} - 10^{14}\, W/cm^2$ for 800 nm pulses for the sub-100 fs regime [10]. The plasma density is also clamped due to the sudden reversal of the self-focusing process. Densities between 10^{12} and 10^{18} cm^{-3} have been reported [43, 44]. Such a broad range of values is a consequence of the initial pulse energy, width, and

focusing conditions [35, 45]. The self-consistent collapse of a filament and the conservation of its characteristics during propagation lead to beam regularization, referred to as self-cleaning. The profile emerging after collapse has been shown to be symmetric despite non-symmetric inputs [46]. The Townes structure is also important because the core and reservoir work together. For example, the core will diffract upon disruption of the reservoir [37,38]. However, depletion of the core through absorption or an obstacle will not necessarily destroy the filament. Instead, the supporting photon bath will replenish the core in a self-healing process [38, 47-52]. Together, these unique properties allow filamenting beams to propagate long distances in a robust manner. Plasma channels just under 400 meters have been sustained by properly adjusting the beam's initial temporal chirp [53, 54].

Spectral broadening is also present in femtosecond filaments through the familiar Raman and FWM effects [55-57]. An example of SC generation is given in Fig. 1.4.

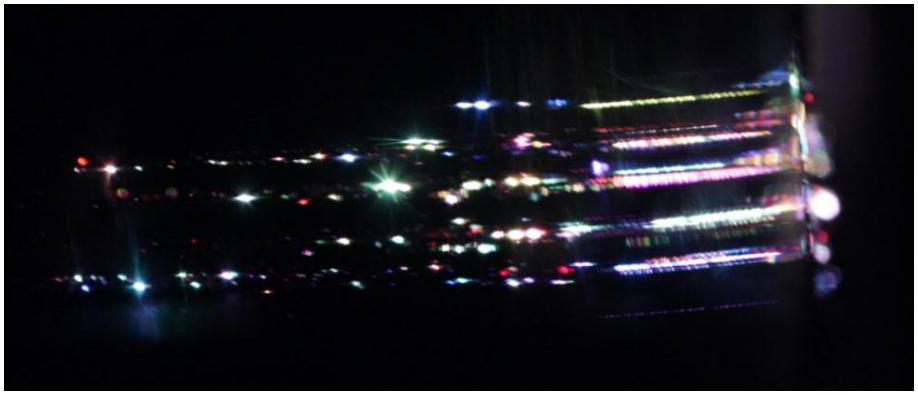

Figure 1.4 – Multiple filaments are shown propagating in a piece of acrylic. Plasma channels are accompanied by SC generation [58].

Larger intensities and wider bandwidths of femtosecond pulses yield broader SC width. This fact, coupled with the effects of SPM and dispersion, cause complex temporal behavior. For example, pulses will self-steepen due to SPM, eventually creating a shock

front and exhibiting bifurcation [59-61]. The addition of non-paraxiality will cause even more severe pulse distortions [62, 63]. These dynamic behaviors have been utilized to generate compressed pulses on the order of a few optical cycles [64].

CHAPTER 2: MEASURING THE KERR NONLINEARITY

The first step in understanding the collapse of a filamenting beam is quantifying the Kerr nonlinearity. In this chapter, the wavefront of a self-focusing beam is characterized before collapse has occurred. The role of the Kerr nonlinearity will be illustrated by correlating the progression of the beam's spatial profile to its wavefront evolution.

2.1 Experimental Setup

The purpose of this experiment was to quantify self-focusing through wavefront measurements. The laser used was the multi-terawatt femtosecond laser (MTFL) at University of Central Florida's Laser Plasma Laboratory [65]. This system uses a Ti:sapphire chirp-pulse amplification architecture, shown in Fig. 2.1 [34].

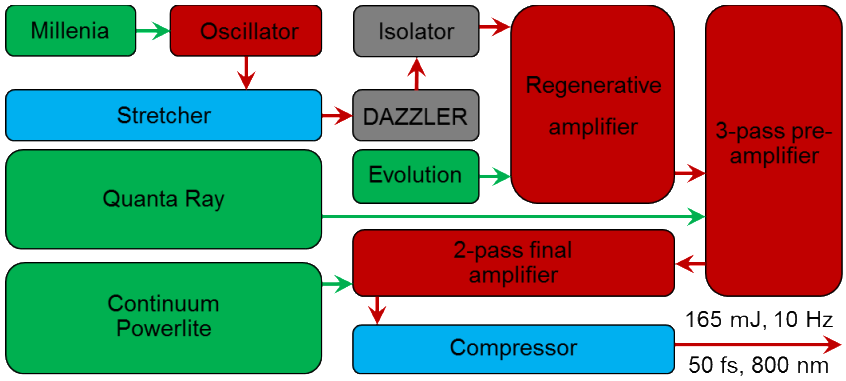

Figure 2.1 – The MTFL system uses chirp-pulse amplification to achieve terawatt level pulses at 10 Hz centered at 800 nm.

The output was collimated with an approximately transform-limited pulse duration of 60 fs and a diameter ($1/e^2$) of 14 mm. The frequency-resolved optical gating (GRENOUILLE [66]) technique was used to characterize the pulse width as shown in Fig. 2.2.

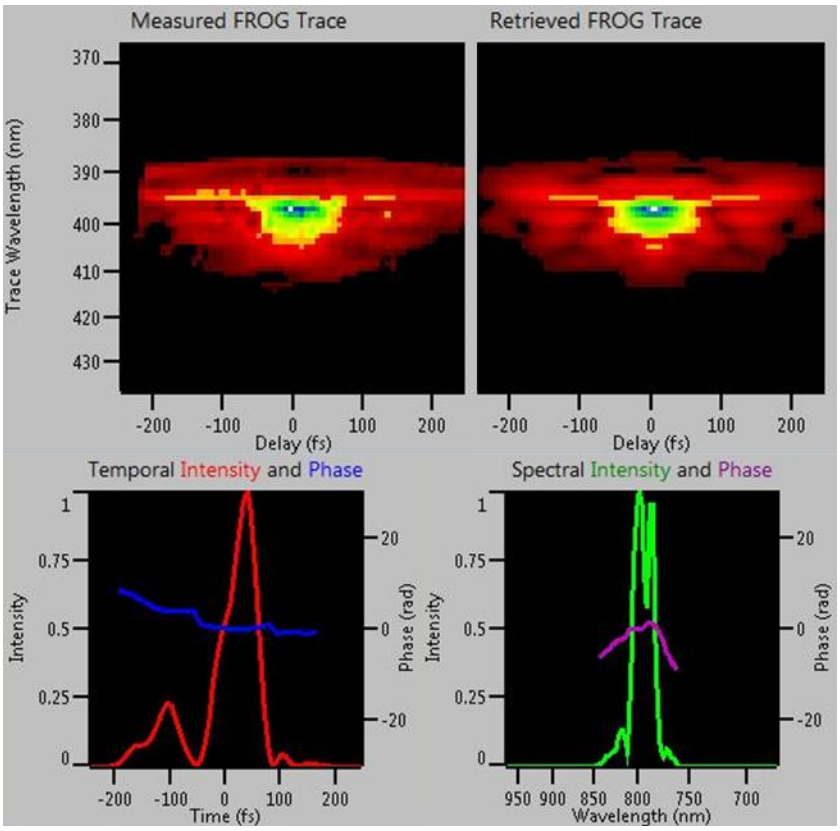

Figure 2.2 – a) Measured and b) retrieved GRENOIULLE spectrograms. c) Temporal and d) spectral retrievals

The beam was allowed to freely propagate for pulse energies up to 9 mJ. Wavefront and beam profile measurements were taken 5.6 m from the output of the laser. At this range, self-focusing is the dominant mechanism. According to Eq. 2.2, the self-collapse location of a 9 mJ beam 14 mm in diameter with a pulse width of 60 fs is ~15 m. Therefore, it is acceptable to only account for the Kerr contribution to the beam's wavefront. The beam was imaged after propagating 5.6 m. Two large optical wedges (W1 and W2) were used to reduce intensity as much as possible while avoiding material damage, as shown in Fig. 2.3. Another two wedges were used in a periscope (PS) to further reduce intensity. The beam was then de-magnified by a factor of 5 using a 4-F telescope, allowing the whole

beam to be directly measured using either a Shack-Hartmann wavefront sensor (SHWFS) or a CCD [67].

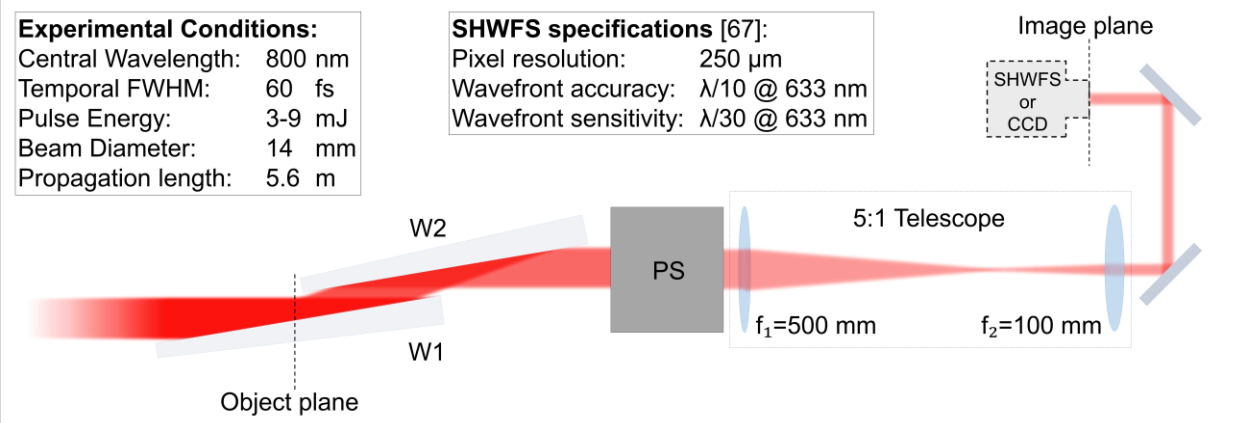

Figure 2.3 – The experimental setup used for measuring wavefront profile and experimental conditions is shown. Two large wedges are followed by 2 inch wedges in a periscope in order to arrest the nonlinear collapse. The plane of the first wedge is imaged at the detector plane with a magnification of 5:1.

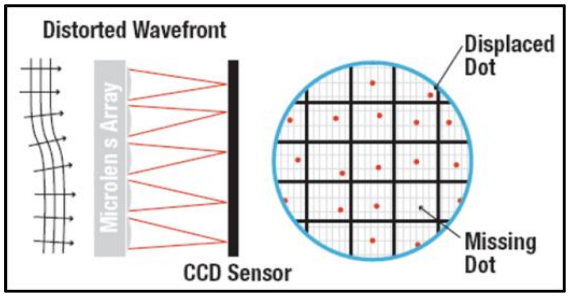

Figure 2.4 – The operation principle of the SHWFS [67]. A microlens array is used to spatially sample the wavefront. The incident wavefront distortions translate to displaced images on the CCD array.

The operating principle of the SHWFS is shown in Fig. 2.4. The sensor plane of the SWHFS was placed in the Fourier plane of the second lens (f_2=100 mm); the first surface of W1 was placed at the Fourier plane of the first lens (f_1=500 mm). Satisfaction of the 4-F imaging condition was verified by placing a needle on the surface of the first wedge and optimizing the resolution of the needle tip. An example of the measured intensity and wavefront data is shown in Fig. 2.5.

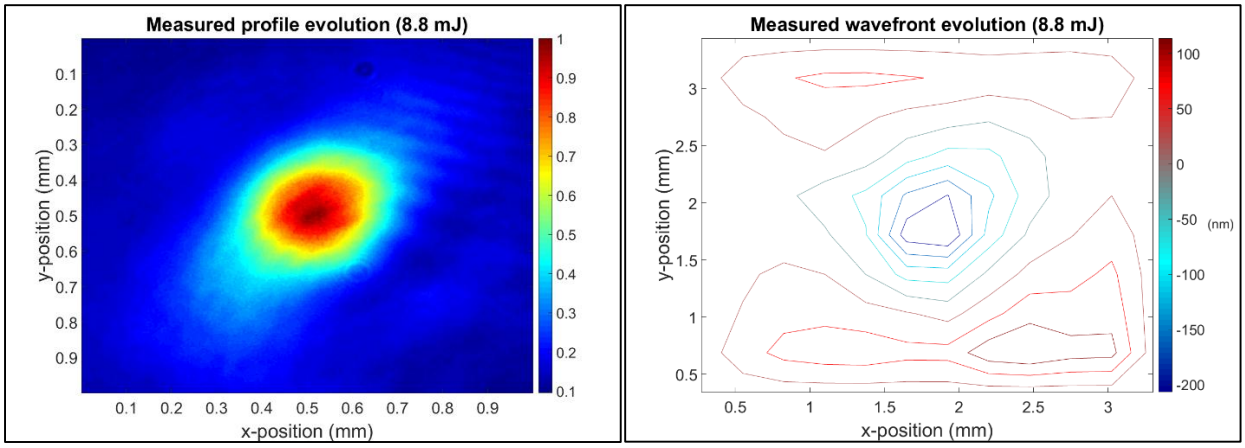

Figure 2.5 – An example a measurement of the beam profile (left) and wavefront (right) is given for an 8.8 mJ pulse. The spatial scales correspond to the detectors. No corrections have been made based on magnification.

2.2 Profile and Wavefront Measurements

The first part of this study examined the progression of a beam's wavefront profile in the pre-filamentation regime. This was done primarily as a proof-of-concept, validating the ability to accurately characterize an arbitrary wavefront. The data was also useful for qualitatively understanding the Kerr self-focusing process. A simple model was used to understand beam evolution under pre-collapse conditions. The χ^3 term of the electronic susceptibility gives rise to the Kerr nonlinearity which alters the refractive index of the medium according to the intensity profile of a propagating beam. The beam will then accumulate a corresponding spatially dependent phase based upon the self-induced index modifications.

The evolution of the beam profile and the wavefront shape are measured against the input pulse energy (at a fixed distance of z=5.6 m) using the described setup shown in Fig. 2.3. Figure 2.6 shows the full beam profiles at highest and lowest pulse energies used. A comparison of these two images shows the overall effect of self-focusing on beam shape.

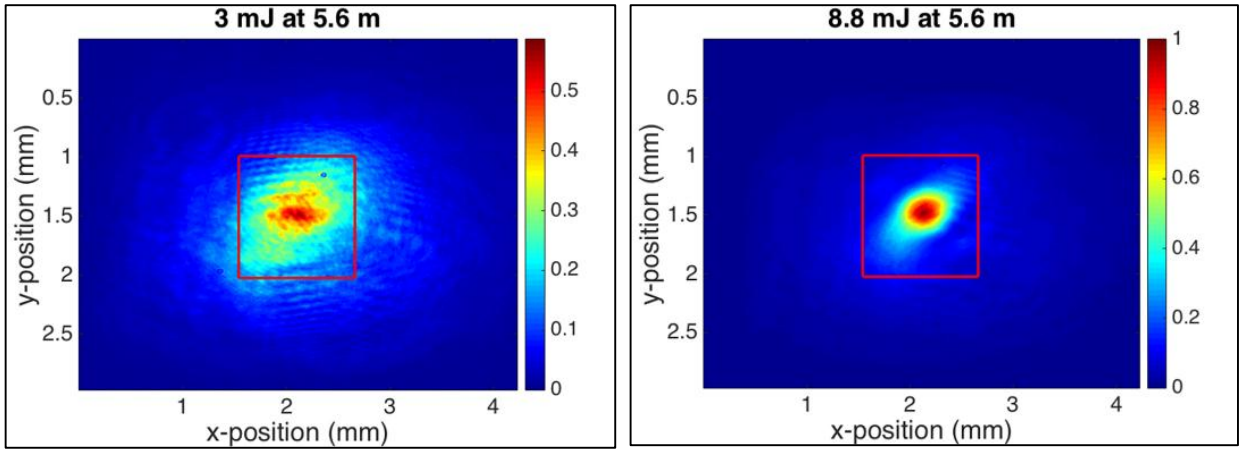

Figure 2.6 – The final beam profiles at 5.6 m for the poorly conditioned case for 3 mJ (left) and 8.8 mJ (right). The Kerr effect builds up quickly even at short distances due to the initial beam shape.

The full results are shown in Fig. 2.7 and 2.8. The red box indicates the region of interest plotted in Fig. 2.7. The normalized beam profiles show a clear reduction of beam size, indicative of self-focusing.

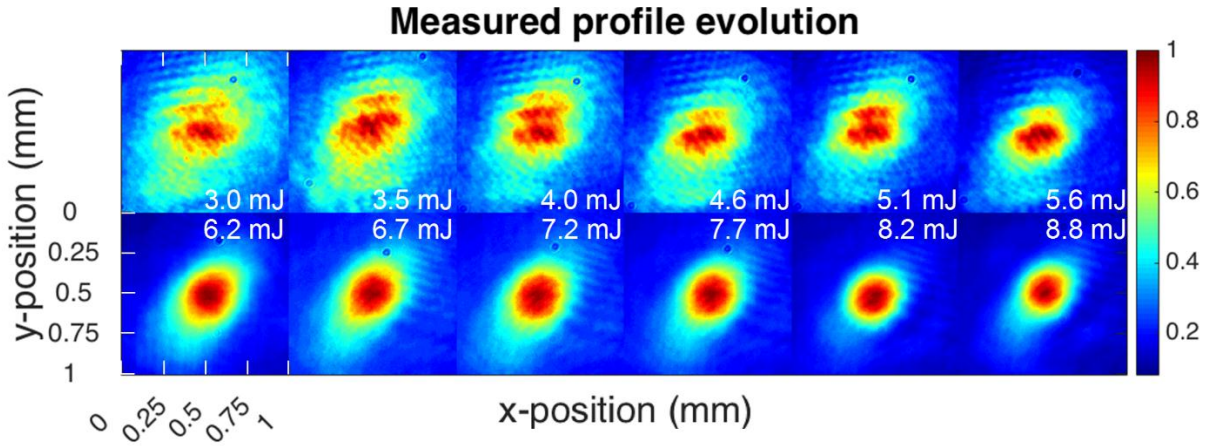

Figure 2.7 – The normalized progression of the hot-spot intensity with increasing energy indicated self-focusing. The pulse energies are indicated in each figure. Each image was taken at the same transverse plane, 5.6 meters from the output of the laser.

Comparing the measured wavefront profiles to irradiance distributions at each energy further validates this point. Figure 2.8 shows the corresponding wavefront profiles after 5.6 meters of propagation. The central wavefront depression is clearly seen to increase

at higher energies where self-focusing is stronger. The increase in the wavefront curvature in turn causes the beam to focus and increase in peak irradiance.

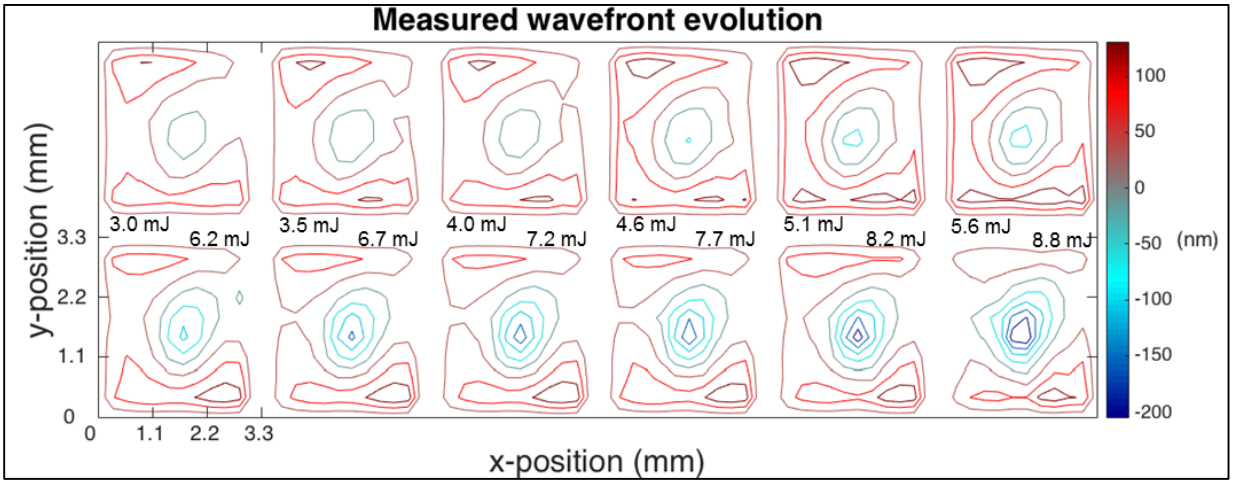

Figure 2.8 – Contour plots of measured beam wavefront are shown for different pulse energies after 5.6 m of propagation. The pulse energies are marked for each profile.

2.3 Confirmation of the Kerr Effect

The Kerr effect was further understood by quantifying the contribution of self-focusing. Equation 2.1 describes the phase accumulation along propagation in terms of the nonlinear refractive index of the medium. This measure is based directly on the definition of Kerr index modification given in Eq. 1.3 (the plasma term is neglected in the pre-collapse regime). Equation 2.2 converts spatial phase $\beta(x,y,Z)$ to optical wavefront path length difference $S(x,y,Z)$. Deviations from a collimated (flat) wavefront are quantified in terms of meters

$$\beta(x,y,Z) = k_0 \int_0^Z n_2 I(x,y,z)\, dz \tag{2.1}$$

$$S(x,y,Z) = \frac{\beta(x,y,Z)}{k_0} \approx n_2 I(x,y,Z) Z \tag{2.2}$$

In general, self-focusing causes a beam to change shape. However, if the beam shape does not change drastically then Eq. 2.2 can be simplified as shown. Laser parameters and measured beam profiles are used to predict wavefront distortion using this equation. A nonlinear index of $n_2 = 2 \cdot 10^{-19}\, cm^2/W$ for air is assumed [4, 5].

A direct numerical comparison between the measured and theoretical results is performed by calculating the "sag" of the wavefront. The sag is defined, in this setting, as the peak-to-valley (PV) wavefront deviation. Such a metric was chosen from the definition adopted in the Zernike polynomial formulation [68]. This choice is appropriate considering the parabolic shape of the wavefront profiles. More complicated shapes would require the use of other Zernike polynomials. The sag was calculated for the measured wavefront data by taking line profiles of the wavefront in the horizontal and vertical directions. The locations of the line profiles were set such that they intersected the extrema of the data (located in the center where intensity is largest). Figures 2.9 and 2.10 show examples of quadratic fits in the horizontal and vertical directions, confirming that the wavefront shape is indeed parabolic.

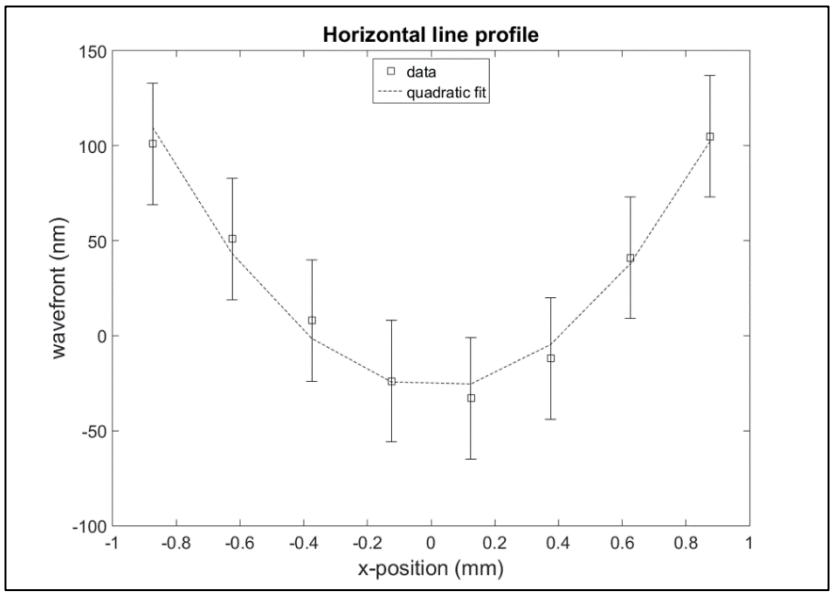

Figure 2.9 – The horizontal line profile through the wavefront minimum for the 3 mJ case. The measured data is shown with the quadratic fit used to calculate the sag.

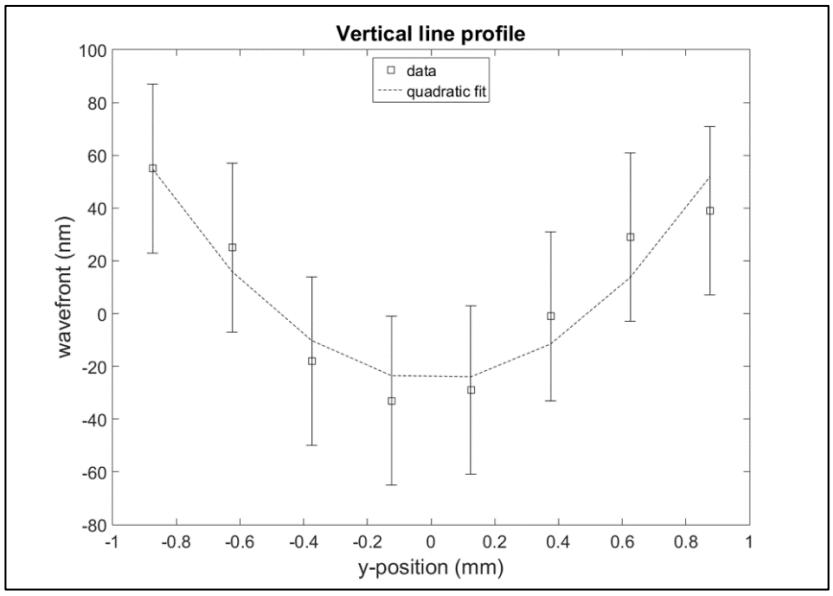

Figure 2.10 – The line profile and quadratic fit in the vertical direction for the 3 mJ case.

The PV was then found for each direction. For the theoretical data, the sag was defined in exactly the same way. The theoretical wavefront profiles were generated using measured beam irradiance profiles, experimental parameters, and Eq. 2.2. The calculated PV

wavefront deviation is plotted alongside the measured values for each pulse energy in Fig. 2.11 and 2.12.

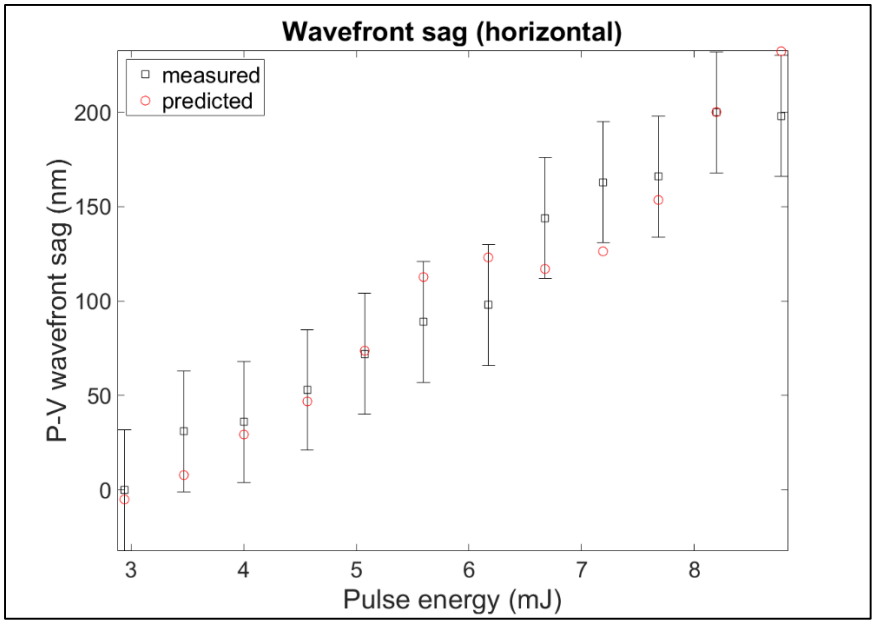

Figure 2.11 – The predicted and measured peak-to-valley sag as a function of pulse energy shows close agreement.

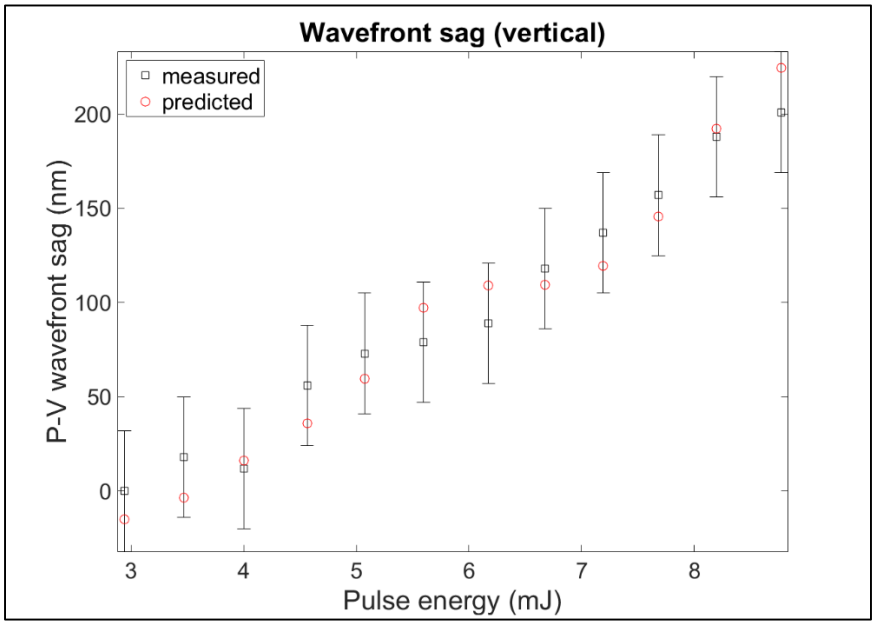

Figure 2.2 – The predicted and measured peak-to-valley sag in the vertical direction.

There is agreement between the measured and predicted sag values within the experimental uncertainty, except for a two cases (in the horizontal data). This is reasonable due to the simplifying assumption made in Eq. 2.2.

These results have verified that the SHWFS measurement method accurately tracks wavefront evolution. The agreement between the measured results and the theory used supports the claim that the Kerr effect is the dominant nonlinearity present at the measurement plane.

CHAPTER 3: WAVEFRONT MEASUREMENTS IN THE FILAMET

The measurements presented in the previous chapter are now extended into the filamentation regime. The wavefront is measured through the collapse region, where plasma generation arrests self-focusing. The wavefront information gathered allows the onset of filamentation to be further defined by correlating spectral broadening and spatial intensity with the presented phase measurements.

3.1 Experimental Setup

The experimental procedure is very similar to that described in the previous chapter, as shown in Fig. 2.3. The input beam was 70 fs and had a $1/e^2$ diameter of approximately 14 mm. The initial beam profile is shown in Fig. 3.1.

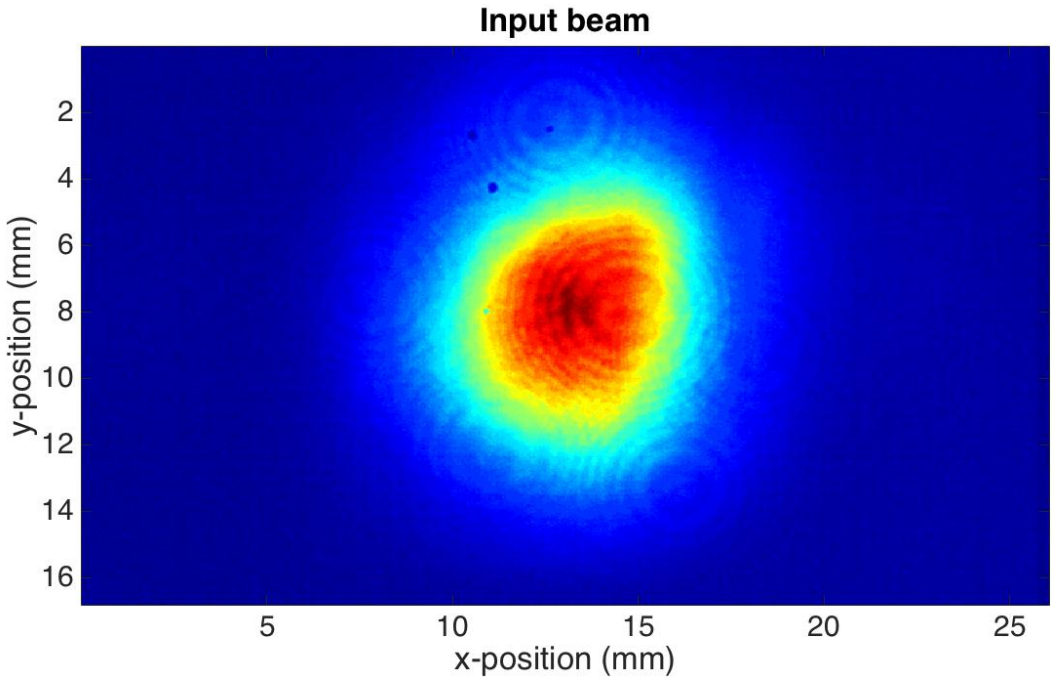

Figure 3.1 – The spatial profile of the input beam is shown in normalized units.

In this case a 10 m lens was used to assist collapse. The measurement plane of the system was translated between 8 m and 10 m from the lens in increments of 25 cm. At

these locations the beam was much smaller than its original size. A 300 mm lens was used to create a 1:1 image of the beam on the imaging plane. Finally, a spectral measurement was added by collecting light transmitted through a wedge with a multimode fiber. Measurements of spatial intensity, wavefront, and spectrum for pulse energies between 1 mJ and 13.5 mJ were taken at each position.

3.2 Identifying the Onset of Filamentation

The addition of a spectral measurement was useful because it helped pinpoint the collapse location of the focused beam. Figure 3.2 shows the progression of the beam's spectrum as a function of distance from the 10 m lens for three different energies.

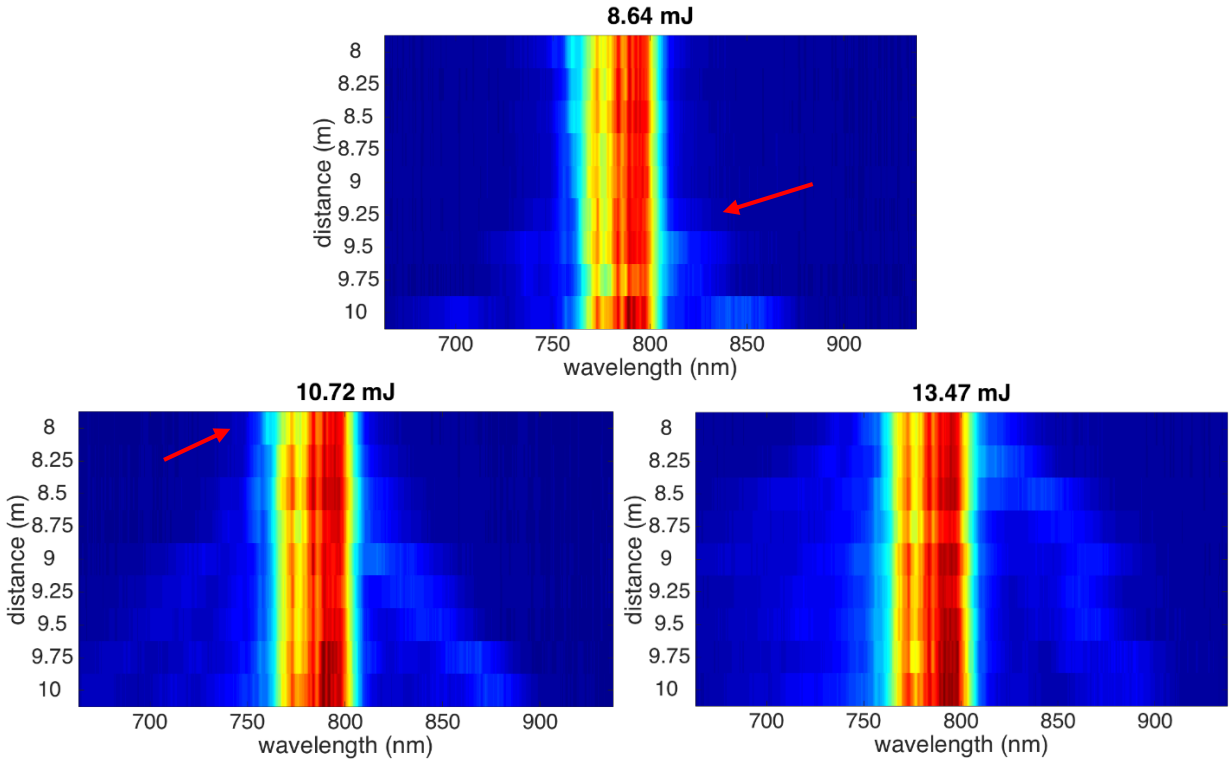

Figure 3.2 – The spectral progression as a function of distance is plotted in dB for three of the measured pulse energies. These plots show that measurements reside both before and after the onset of filamentation. Arrows identify the onset of spectral broadening, used as indication of filament generation.

One well known feature of filaments is spectral broadening, which is clearly present in each image [10]. For each location, the full width at 90% of the peak amplitude was calculated for all energies. The collapse condition was then defined as the energy at which the width increased by a factor of 5%. These conditions are identified with arrows in Fig. 3.2. Note that the spectral evolution at 13.47 mJ does not have an arrow. This is because the threshold for broadening occurs before the shortest distance of 8 m.

3.3 Profile and Wavefront Measurements

The spatial intensity and phase profiles were also measured with respect to energy and propagation distance. Figure 3.3 maps the normalized spatial profile of the beam at each measurement condition.

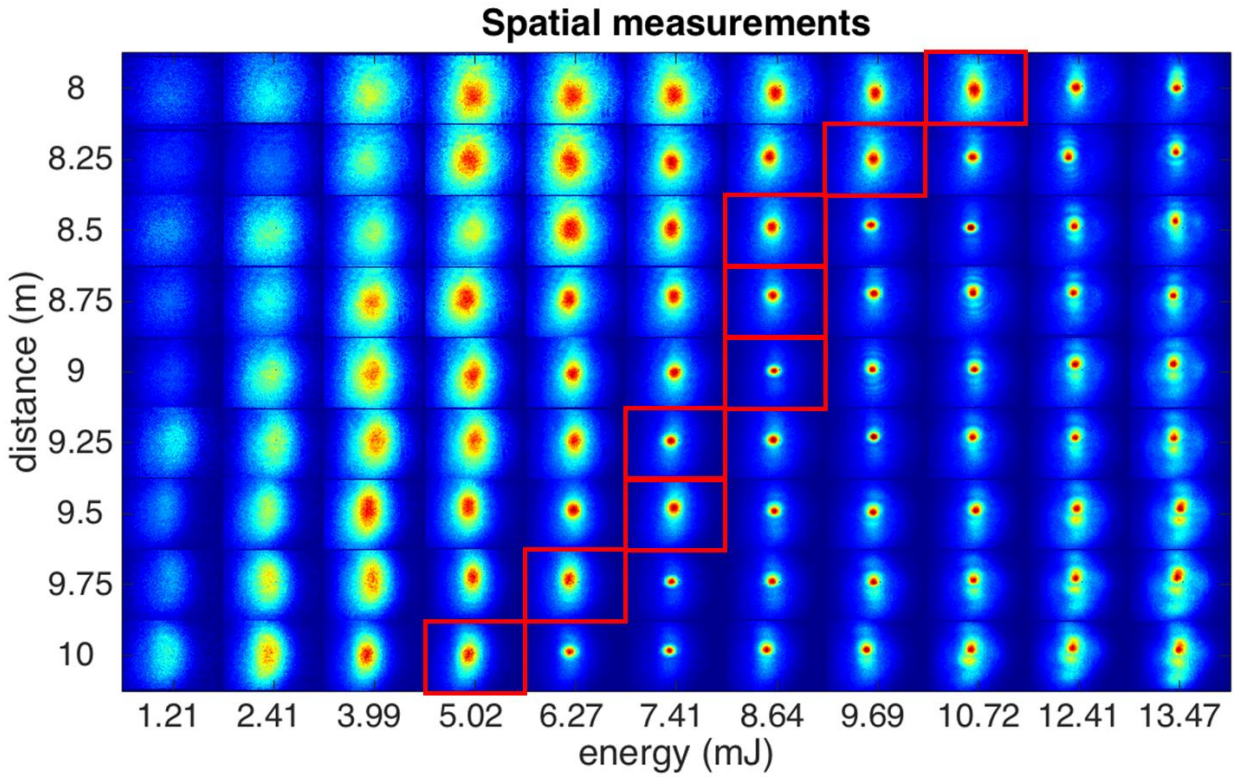

Figure 3.3 – A spatial profile measurement is shown for each condition. For each distance, the threshold energies for broadening were found and are indicated by the red boxes.

The profiles corresponding to the calculated collapse energies for each location are identified. These images show the same pattern as energy and distance are increased. First, the beam's size is reduced. It then forms a singular intensity peak corresponding to the location of initial filament formation. After this point the peak begins to split into multiple peaks. This behavior is consistent with the formation of multiple filaments, which is expected once the critical power of about 5 GW is surpassed. Also note that collapse location is moved to earlier positions at higher energies. This also makes sense since self-focusing occurs more rapidly at increased energies [10]. The spatial profiles are analyzed by numerically calculating the standard deviation, $\sigma_{x,y}$, in both horizontal and vertical directions. Equation 3.1 shows how these values are defined. Contour plots of the beam's horizontal and vertical widths are plotted in Fig. 3.4 as a function of distance and energy.

$$\sigma_x^2 = \langle x^2 \rangle - \langle x \rangle^2 = \frac{\iint_A x^2 I(x,y)dxdy}{\iint_A I(x,y)dxdy} - \left[\frac{\iint_A xI(x,y)dxdy}{\iint_A I(x,y)dxdy}\right]^2 \tag{3.1}$$

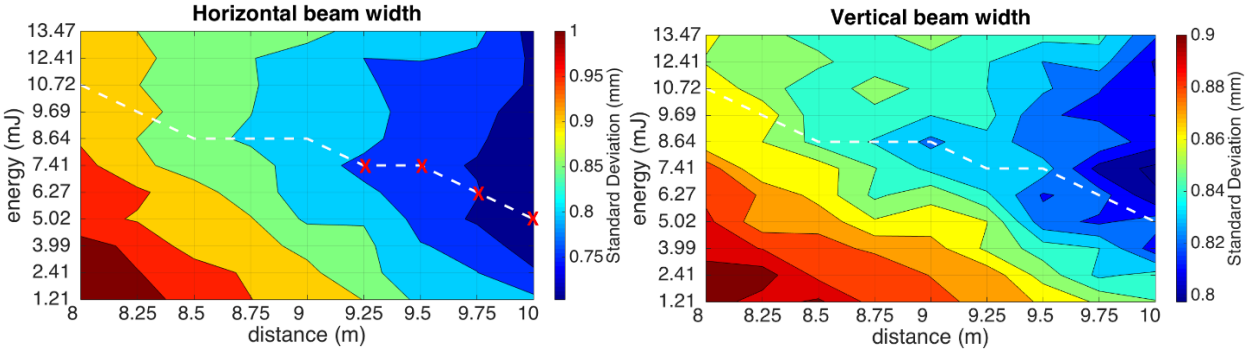

Figure 3.4 – Contour plots of the beam's standard deviation in the horizontal and vertical directions are given. The onset of spectral broadening is marked with the white dashed line and the red X marks indicate conditions that lineouts are plotted for below.

Both plots in Fig. 3.4 show the same trend. However, there are slight inconsistencies in the vertical case where width does not monotonically decay with distance. This can be explained by the spatial intensity break-up observed in the vertical direction as multiple

filamentation begins. The dashed line indicated the onset of spectral broadening. Note that the width at the collapse distance decreases at lower energies. This is better seen in the horizontal line-outs shown in Fig. 3.5. The conditions of each line-out are marked in Fig. 3.4.

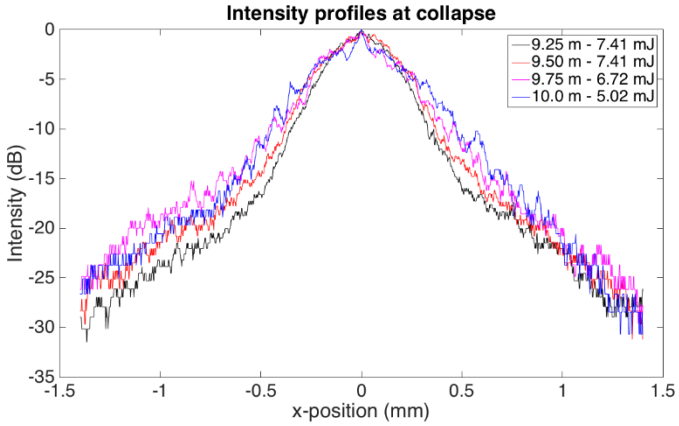

Figure 3.5 – Horizontal line profiles are normalized and plotted in dB for the conditions indicated in Fig. 3.4. Each profile has the same shape, but slightly different width.

A reduced beam width for lower energies at the collapse point makes sense because spectral broadening is driven by nonlinearities, such as ionization and SPM [10, 35, 52]. The intensity dependence of these nonlinearities means they require a reduced beam size if the energy is reduced. Temporal narrowing is another means of conserving intensity and is likely to occur within a filament [62-64]. However, this was not measured in this study and would have to be investigated further. A second feature shown in the line-outs is the relative shape of each profile. It is known that filaments collapse in a self-similar fashion, taking on a Townesian profile after collapse has occurred. These measured profiles have the same qualitative features as a Townesian—a narrow, intense core surrounded by a wide peripheral field—but quantitatively they have a larger width [39, 52]. A single filament is expected to be approximately 400 μm wide at 99% of the peak amplitude

with a peripheral field extending 2 mm in diameter [38]. The wider measured widths are expected due to intensity clamping present in filaments. Since these beams exceed the critical power, it is expected that multiple smaller peaks will form, each carrying a single filament at a clamped intensity. As mentioned above, the onset of multiple filamentation is observed beyond the spectral broadening threshold. However, the observation of the beam's break-up into multiple filaments is only qualitative and not the main focus of this study.

3.4 Wavefront Analysis

The wavefront at each condition was also measured. Figure 3.6 shows an example wavefront measurement.

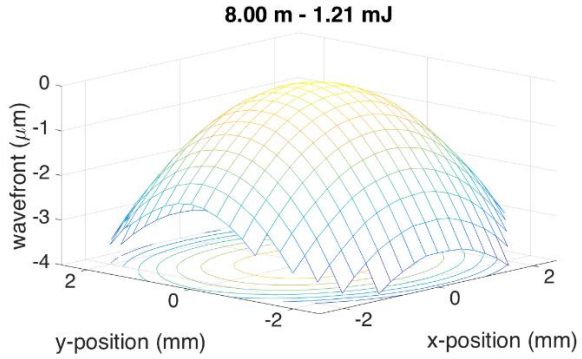

Figure 3.6 – An example of a complete wavefront measurement. Each profile has the same shape, but a different curvature.

The wavefront shape is parabolic due to the quadratic phase of the 10 m lens. This is confirmed by the line-outs shown of Fig. 3.6, shown in Fig. 3.7 and fitted to a second order polynomial. The analysis performed uses the second derivative of the polynomial fit to calculate the curvature of the wavefront at the center of the profile.

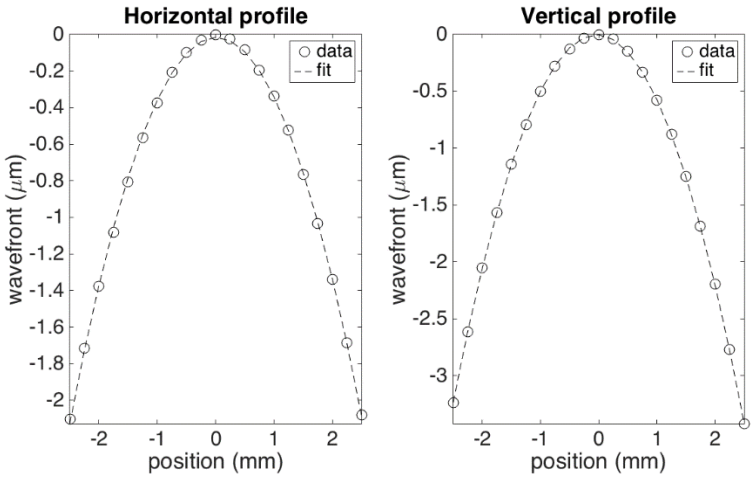

Figure 3.7 – The vertical and horizontal line-outs of the wavefront shown in Fig. 3.6 are shown along with their quadratic fit.

The polynomial fit takes the form shown in Eq. 3.2 and the second derivative is easily defined. The curvature is then defined at the center of the wavefront (x=0) by Eq. 3.3.

$$f(x) = a_2 x^2 + a_1 x + a_0 \tag{3.2}$$

$$f''(x) = 2a_2$$

$$\kappa = \frac{f''(x)}{(1+[f'(x)]^2)^{\frac{3}{2}}} = 2a_2 \; at \; x = 0 \tag{3.3}$$

Figure 3.8 maps the curvature for each experimental condition. Negative curvatures correspond to focusing while positive curvatures indicate defocusing [67]. The data shows that the conditions where broadening begins match precisely with the points of maximum positive wavefront curvature (maximum defocusing). Additionally, the curvature drops again after the collapse location for each energy, indicating a return to a focusing profile.

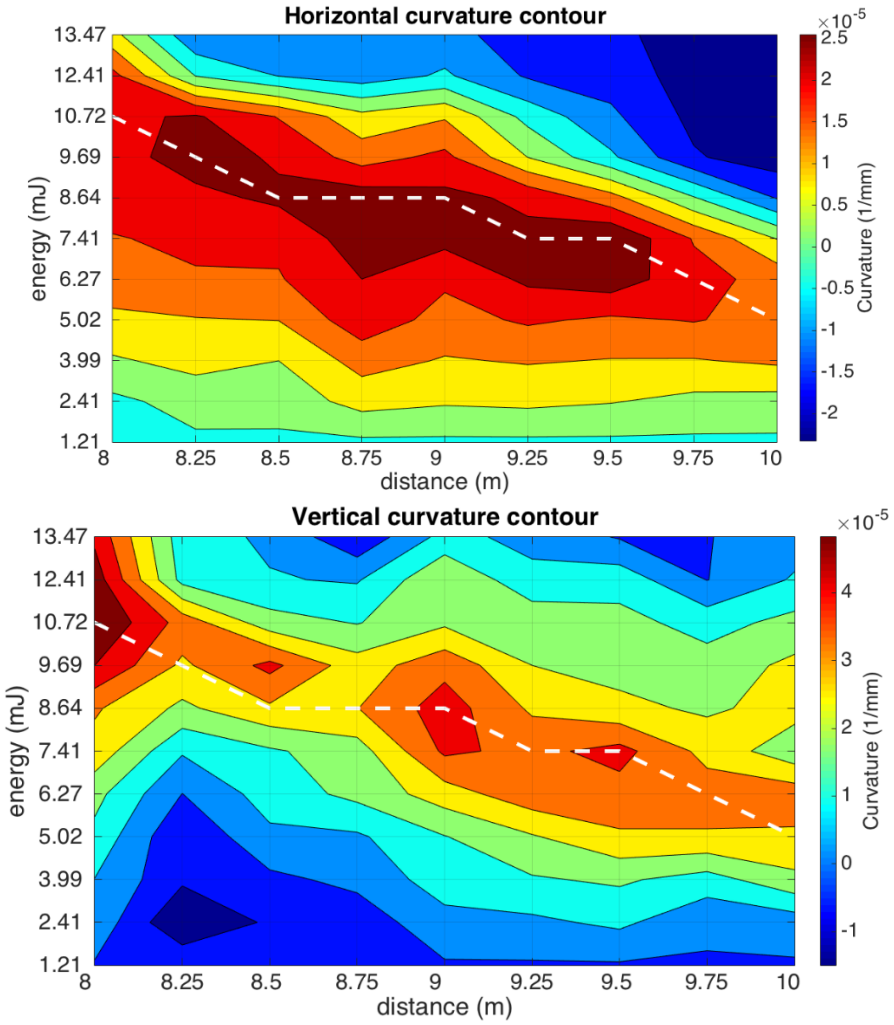

Figure 3.8 – The wavefront curvature is plotted for both horizontal and vertical line profiles of each wavefront. The onset of spectral broadening is marked with the dashed line and corresponds closely to where curvature is greatest.

This is the opposite of what would happen for a linearly focused beam, which transitions from negative to positive curvature, remaining positive after it passes through focus. Here, however, curvature does not continue to increase in the positive direction after collapse. This behavior can be explained in terms of plasma generation, followed by self-focusing. As the beam initially self-focuses, plasma generation will suddenly begin since MPA scales as I^8 in air [10]. This will reduce the index of refraction in the center of the beam where the plasma density is greatest, resulting in an increase in curvature in the positive

direction. This reduction in refractive index combats self-focusing and the rate of energy convergence is reduced. This is reflected in the beam width contours shown in Fig. 3.4. The separation between contour lines increases after the onset of spectral broadening. Additionally, the energy in the main peaks observed in Fig. 3.3 begins to migrate into adjacent hot-spots, while the initial intensity peak remains relatively constant in size. A reduction in energy concentration will then reduce the ionization rate and plasma defocusing will play a less significant role. A decrease in the wavefront curvature at distances after (to the right of) the main peak in Fig. 3.8 verifies this expectation. At this point, the self-focusing process begins to re-appear and the filament becomes fully established. Finally, it is also expected that the sudden onset of plasma generation would be accompanied by the onset of spectral broadening since plasma generation and the nonlinearities responsible for the spectral broadening (SPM, FWM, self-steepening) require high peak intensities. Multiple other works have confirmed this both theoretically and experimentally [10, 35, 52, 64].

CONCLUSION

This work has provided characterization of the filamentation process through measurements of spatial wavefronts. The two competing processes in a filament have been examined separately. First, Kerr self-focusing was measured for a beam in the pre-filament regime as a function of input energy. A comparison of experimental data and theoretical predictions showed agreement between the measured evolution of both wavefront and spatial profile. Next, the wavefront of a beam in the filament regime was probed. Here, the contribution of plasma defocusing was expressed as a peak in wavefront curvature. This peak corresponded to other indicators of filament onset, specifically spectral broadening, formation of the Townesian profile, and the initial formation of multiple filaments. Finally, the wavefront curvature was observed to decrease after the peak associated with plasma defocusing, indicating the return of the self-focusing process. Thus, measurements in this study cover the initial self-focusing process, the plasma generation at the onset of filamentation, and the return to self-focusing after the filament has been established. Further work will carry out these measurements with higher spatial resolution and at further distances in order to better resolve the competition between self-focusing plasma defocusing throughout the length of the filament.

REFERENCES

[1] R. Y. Chao, E. Garmire, and C. H. Townes, “Self-trapping of optical beams,” Phys. Rev. Lett. **13**, 15 (1964).

[2] P. L. Kelley, “Self-focusing of optical beams,” Phys. Rev. Lett. **15**, 26 (1965).

[3] G. Fibich and A. L. Gaeta, "Critical power for self-focusing in bulk media and in hollow waveguides," Opt. Lett. **25**, 5 (2000).

[4] E. T. J. Nibbering, G. Grillon, M. A. Franco, B. S. Prade, and A. Mysyrowicz, “Determination of the inertial contribution to the nonlinear refractive index of air, N_2, and O_2 by use of unfocused high-intensity femtosecond laser pulses,” J. Opt. Soc. Am. B **14**, 3 (1997).

[5] V. Loriot, E. Hertz, O. Faucher, and B. Lavorel, “Measurement of high order Kerr refractive index of major air components,” Opt. Exp. **17**, 16 (2009).

[6] W. Liu and S. L. Chin, “Direct measurement of the critical power of femtosecond Ti:sapphire laser pulse in air,” Opt. Exp. **13**, 15 (2005).

[7] E. L. Dawes and J. H. Marburger, “Computer studies in self-focusing,” Phys. Rev. **179**, 3 (1969).

[8] J. H. Marburger, “Self-focusing: Theory,” Prog. Quant. Electr. **4**, 1 (1975).

[9] G. Fibich, “Adiabatic law for self-focusing of optical beams” Opt. Lett. **21**, 21 (1996).

[10] A. Couairon and A. Mysyrowicz, “Femtosecond filamentation in transparent media,” Phys. Rep. **441**, 2—4 (2007).

[11] E. Yablonovitch and N. Bloembergen, “Avalanche ionization and the limiting diameter of filaments induced by light pulses in transparent media,” Phys. Rev. Lett. **29**, 14 (1972).

[12] A. Couairon and L. Bergé, “Light Filaments in Air for Ultraviolet and Infrared Wavelengths,” Phys. Rev. Lett. **88**, 13 (2002).

[13] L. V. Keldysh, “Ionization in the field of a strong electromagnetic wave,” Sov. Phys. JETP **20**, 5 (1965).

[14] A. Couairon, S. Tzortzakis, L. Bergé, et al., “Infrared femtosecond light filaments in air: simulations and experiments,” J. Opt. Soc. Am. B, **19**, 5 (2002).

[15] F. J. McClung and R. W. Hellwarth, “Giant optical pulsations from ruby,” J. Appl. Phys. **33**, 3 (1962).

[16] E. Garmire, R. Y. Chao, and C. H. Townes, “Dynamics and characteristics of the self-trapping of intense light beams,” Phys. Rev. Lett. **16**, 9 (1966).

[17] Y. R. Shen and Y. J. Shaham, “Beam deterioration and stimulated Raman effect,” Phys. Rev. Lett. **15**, 26 (1965).

[18] P. Lallemand and N. Bloembergen, “Self-focusing of laser beams and stimulated Raman gain in liquids,” Phys. Rev. Lett. **15**, 26 (1965).

[19] N. Bloembergen, P. Lallemand, and A. Pine, “The influence of self-focusing on the stimulated Brillouin, Raman, and Rayleigh effects,” IEEE J. Quant. Elect. **2**, 8 (1966).

[20] C. C. Wang, “Length-dependent threshold for stimulated Raman effect and self-focusing of laser beams in liquids,” Phys. Rev. Lett. **16**, 9 (1966).

[21] M. M. T. Loy and Y. R. Shen, “Study of self-focusing and small-scall filaments of light in nonlinear media,” IEEE J. Quant. Elect. **9**, 3 (1973).

[22] R. L. Carman, R. Y. Chiao, and P. L. Kelley, “Observation of degenerate stimulated four-photon interaction and four-wave parametric amplification,” Phys. Rev. Lett. **17**, 26 (1966).

[23] L. Brillouin, “Diffusion de la lumière et des rayonnes X par un corps transparent homogéne; Influence del´agitation thermique”, Ann. Phys. **17**, 88 (1922)

[24] Y. R. Shen and N. Bloembergen, “Theory of stimulated Brillouin and Raman scattering,” Phys. Rev. **137**, 6A (1965).

[25] C. V. Raman, “A new radiation,” Indian J. Phys. **2**, (1928).

[26] S. A. Akhmanov, A. P. Sukhorukov, and R. V. Khokhlov, “Self-focusing and diffraction of light in a nonlinear medium,” Sov. Phys. –Usp. **93**, 1–2 (1966).

[27] A. J. Campillo, S. L. Shapiro, and B. R. Suydam, “Periodic breakup of optical beams due to self-focusing,” Appl. Phys. Lett. **23**, 11 (1973).

[28] A. J. Campillo, S. L. Shapiro, and B. R. Suydam, “Relationship of self-focusing to spatial instability modes,” Appl. Phys. Lett. **24**, 4 (1974).

[29] F. Shimizu, “Frequency broadening in liquids by a short light pulse,” Phys. Rev. Lett. **19**, 19 (1967).

[30] R. R. Alfano and S. L. Shapiro, “Observation of self-phase modulation and small-scale filaments in crystals and glasses,” Phys Rev. Lett. **24**, 11 (1970).

[31] R. R. Alfano and S. L. Shapiro, “Emission in the region 4000 to 7000 Å via four-photon coupling in glass,” Phys. Rev. Lett. **24**, 11 (1970).

[32] S. L. Chin, S. A. Hosseini, W. Liu, Q. Luo, F. Théberge, N Aközbek, A. Becker, V. P. Kandidov, O. G. Kosareva, and H. Schroeder, “The propagation of power femtosecond laser pulses in optical media: physics, applications, and new challenges,” Can. J. Phys. **83**, 9 (2005).

[33] A. Braun, G. Korn, X. Liu, D. Du, J. Squier, and G. Mourou, “Self-channeling of high-peak-power femtosecond laser pulses in air,” Opt. Lett. **20**, 1 (1995).

[34] D. Strickland and G. Mourou, “Compression of amplified chirped optical pulses,” Opt. Comm. **56**, 3 (1985).

[35] K. Lim, “Laser filamentation – beyond self-focusing and plasma defocusing (Ph.D. Thesis),” University of Central Florida, (2014).

[36] A. Brodeur, C. Chien, F. Ilkov, and S. Chin, "Moving focus in the propagation of ultrashort laser pulses in air," Opt. Lett. **22**, 5 (1997).

[37] W. Liu, J. –F. Gravel, F. Théberge, A. Brecker, and S. L. Chin, “Background reservoir: its crucial role for long-distance propagation of femtosecond laser pulses in air,” Appl. Phys. B **80**, 7 (2005).

[38] R. Bernath, “High-intensity ultra-fast laser interaction technologies (Ph.D. Thesis),” University of Central Florida, (2007).

[39] K. D. Moll and A. L. Gaeta, “Self-similar optical wave collapse: Observation of the Townes profile,” Phys. Rev. Lett. **90**, 20 (2003).

[40] R. Rankin, C. E. Capjack, N. H. Burnett, and P. B. Corkum, “Refraction effects associated with multiphoton ionization and ultrashort-pulse laser propagation in plasma waveguides,” Opt. Lett. **16**, 11 (1991).

[41] J. Kasparian, R. Sauerbrey, and S. L. Chin, “The critical laser intensity of self-guided light filaments in air,” Appl. Phys. B **71**, 6 (2000).

[42] V. Kandidov, V. Fedorov, O. Tverskoy, O. Kossareva, and S. Chin, "Intensity clamping in the filament of femtosecond laser radiation," Quant. Elect. **41**, 4 (2011).

[43] H. Schillinger, R. Sauerbrey, “Electrical conductivity of long plasma channels in air generated by self-guided femtosecond laser pulses,” Appl. Phys. B **68**, 4 (1999).

[44] H. Yang, J. Zhang, W. Yu, Y. J. Li, and Z. Y. Wei, “Long plasma channels generated by femtosecond laser pulses,” Phys. Rev. E **65**, 1 (2002).

[45] F. Théberge, W. Liu, P.T. Simard, A. Becker, and S. L. Chin, “Plasma density inside a femtosecond laser filament in air: Strong dependence on external focusing,” Phys. Rev. E **74**, 3 (2006).

[46] B. Prade, M. France, A. Mysyrowicz, A. Couairon, H. Buersing, B. Eberle, M. Krenz, D. Seiffer, and O. Vasseur, “Spatial mode cleaning by femtosecond filamentation in air,” Opt. Lett. **31**, 17 (2006).

[47] M. Mlejnek, E. M. Wright, and J. V. Moloney, “Dynamic spatial replenishment of femtosecond pulses propagating in air,” Opt. Lett. **23**, 5 (1998).

[48] F. Courvoisier, V. Boutou, J. Kasparian, E. Salmon, G. Méjean, J. Yu, and J. –P. Wolf, “Ultraintense light filaments transmitted through clouds,” Appl. Phys. Lett. **83**, 2 (2003).

[49] M. Kolesik and J. Moloney, “Self-healing femtosecond light filaments,” Opt. Lett. **29**, 6 (2004).

[50] A. Dubietis, E. Kučinskas, G. Tamošauskas, and E. Gaižauskas, “Self-reconstruction of light filaments,” Opt. Lett. **29**, 24 (2004).

[51] G. Méchain, G. Méjean, R. Ackermann, P. Rohwetter, Y. –B. André, J. Kasparian, B. Prade, K. Stelmaszczyk, J. Yu, E. Salmon, W. Winn. L. A. Schilie, A. Mysyrowicz, R. Sauerbrey, L. Wöste, and J. –P. Wolf, “Propagation of fs TW laser filaments in adverse atmospheric conditions,” Appl. Phys. B **80**, 7 (2005).

[52] C. Jeon, “Laser filament interaction with aerosols and clouds (Ph.D. Thesis),” University of Central Florida, (2016).

[53] G. Méchain, C. D’Amico, Y. –B. André, S. Tzortzakis, M. Franco, B. Prade, A. Mysyrowicz, A. Couairon, E. Salmon, and R. Sauerbrey, “Range of plasma filaments created in air by a multi-terawatt femtosecond laser,” Opt. Comm. **247**, 1-3, (2005).

[54] M. Durand, A. Houard, B. Prade, A. Mysyrowicz, A. Durécu, D. Fleury, O. Vasseur, H. Borchert, K. Diener, R. Schmitt, F. Théberge, M. Chateauneuf, J. –F. Daigle, and J. Dubois, “Kilometer range filamentation,” Opt. Exp. **21**, 22 (2013).

[55] P. B. Corkum and C. Rolland, “Femtosecond continua produced in gases,” IEEE J. Quant. Elect. **25**, 12 (1989).

[56] J. Kasparian, R. Sauerbrey, D. Mondelain, S. Niedermeier, J. Yu, J. –P. Wolf, Y. –B. André, M. Franco, B. Prade, S. Tzortzakis, A. Mysyrozicz, M. Rodriguez, H. Wille, and L. Wöste, “Infrared extension of the supercontinuum generated by femtosecond terawatt laser pulses propagating in the atmosphere,” Opt. Lett. **25**, 18 (2000).

[57] S. Petit, A. Talebpour, A. Proulx, and S. L. Chin, “Some consequences during the propagation of an intense femtosecond laser pulse in transparent optical media: a strongly deformed white-light laser,” Las. Phys. **10**, 1 (2000).

[58] N. Barbieri, *Optics & Photonics News*, The Optical Society (2015).

[59] F. DeMartini, C. H. Townes, T. K. Gustafson, and P. L. Kelley, “Self-steepening of light pulses,” Phys. Rev. **164**, 2 (1967).

[60] J. E. Rothenberg, “Pulse splitting during self-focusing in normally dispersive media,” Opt. Lett. **17**, 8 (1992).

[61] J. E. Rothenberg, “Space—time focusing: breakdown of the slowly varying envelope approximation in the self-focusing of femtosecond pulses,” Opt. Lett. **17**, 19 (1992).

[62] G. Fibich and G. C. Papanicolaou, “Self-focusing in the presence of small time dispersion and nonparaxiality,” Opt. Lett. **22**, 18 (1997).

[63] J. K. Ranka and A. L. Gaeta, “Breakdown of the slowly varying envelope approximation in the self-focusing of ultrashort pulses,” Opt. Lett. **23**, 7 (1998).

[64] A. Couairon, J. Biegert, C. P. Hauri, W. Kornelis, F. W. Helbing, U. Keller, and A. Mysyrowicz, “Self-compression of ultra-short laser pulses down to one optical cycle by filamentation,” J. Mod. Opt. **53**, 1-2 (2006).

[65] B. Webb, J. Bradford, K. Lim, N. Bodnar, A. Vaupel, E. McKee, M. Baudelet, M. M. Durand, L. Shah, and M. Richardson, “Compact 10 TW laser to generate multi-filament arrays,” CLEO, San Jose, California, paper SM1F.6 (2014).

[66] P. O’Shea, M. Kimmel, X. Gu, and R. Trebino, “Highly simplified device for ultrashort-pulse measurement,” Opt. Lett. **26**, 12 (2001).

[67] Optical Wavefront Sensors (Shack-Hartmann) Operation Manual. ThorLabs GmbH. (2014).

[68] M. Born and E. Wolf, Principles of Optics (Pergamon Press, New York, 1959).